Engineering Fracture Mechanics 293 (2023) 109718

Contents lists available at ScienceDirect

Engineering Fracture Mechanics

journal homepage: www.elsevier.com/locate/engfracmech

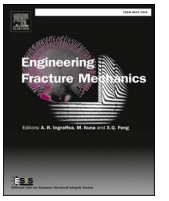

A study on microcrack monitoring in concrete: discrete element method simulations of acoustic emission for non-destructive diagnostics

Magdalena Rucka [a,*], Magdalena Knak [a], Michał Nitka [b]

[a] Department of Mechanics of Materials and Structures, Faculty of Civil and Environmental Engineering, Gdańsk University of Technology, Narutowicza 11/12, 80-233, Gdańsk, Poland

[b] Department of Engineering Structures, Faculty of Civil and Environmental Engineering, Gdańsk University of Technology, Narutowicza 11/12, 80-233, Gdańsk, Poland

ARTICLE INFO

Keywords:
Fracture monitoring
Non-destructive testing (NDT)
Discrete element method (DEM)
Acoustic emission
Concrete beams

ABSTRACT

The research is focused on the monitoring of fracture evolution in concrete beams under three-point bending using the acoustic emission technique and the discrete element method. The main objective of the study was to numerically and experimentally investigate the mechanism behind the generation of elastic waves during acoustic emission events and their interaction with micro- and macro-cracking in concrete beams under monotonic quasi-static loading. This was achieved through the development of a DEM model and numerical modelling of AE effects. An improved 4-phase DEM model of concrete including real mesostructured specimens and the ability to simulate aggregate breakage was introduced. The propagation of elastic waves, recorded in both laboratory experiments and numerical calculations, was given particular attention. The results showed the high suitability of the developed DEM model for monitoring crack initiation, development and propagation, as well as for supporting the interpretation of diagnostic results obtained by acoustic emission techniques.

1. Introduction

Concrete is one of the most widely used building materials in the world. It has a random and multiphase structure. Its main constituents are cement, aggregate, macro-pores and porous interfacial transition zones (ITZs). Due to the brittle or quasi-brittle (depending on the scale, even ductile response is possible [1,2]) nature of concrete, cracking is a phenomenon of prime importance in the design and use of structures made of cement composites. During fracture, micro-cracks initially form in hardening and mainly in the softening region of the stress–strain curve and then develop into dominant, distinct macro-cracks as the material softens. The fracture process in concrete is strictly related to its heterogeneous structure and it is governed by the formation and propagation of the fracture process zone [3]. In order to characterise concrete behaviour and ensure the safety of concrete and reinforced concrete structures, the detection of cracking at an early stage of loading is of great interest in civil engineering.

In recent years, great progress has been made in the development of new non-destructive techniques applicable to the evaluation of concrete structures. In addition, the latest experimental research has focused on the continuous monitoring of concrete elements

* Corresponding author.
E-mail addresses: magdalena.rucka@pg.edu.pl (M. Rucka), magdalena.knak@pg.edu.pl (M. Knak), michal.nitka@pg.edu.pl (M. Nitka).

https://doi.org/10.1016/j.engfracmech.2023.109718
Received 19 June 2023; Received in revised form 24 October 2023; Accepted 2 November 2023
Available online 7 November 2023

subjected to mechanical degradation caused by monotonically increasing loading. One of the most efficient approaches for real-time, in-situ monitoring of the formation of micro-crack zones in concrete is the acoustic emission (AE) method. It is defined as the phenomenon of the release of strain energy as a result of fracture or excessive deformation of a material. As a consequence of such an event, elastic waves are generated which propagate through the material. The AE events can then be detected by sensors that are distributed over the surface of a sample being tested. Information on the initiation and propagation of micro-cracks and fractures in externally stressed specimens can be obtained by analysing the characteristics of the AE signals. Many researchers have addressed the issue of AE-based damage detection in concrete elements. Katsaga et al. [4] employed the AE technique to investigate the process of fracture formation in large, shear-critical, reinforced concrete beams. The influence of concrete mesostructure on shear fracture formation and propagation was studied. Aggelis et al. [5] characterised the fracture process of steel fibre-reinforced concrete using acoustic emission. They found that the amplitude distribution of the AE signals was very sensitive to the micro-cracking in the material. The possibility of classifying different fracture mechanisms of concrete using acoustic emission parameters was discussed by Aggelis in [6]. Vidya Sagar et al. [7] studied different stages of micro-cracking activity of bent concrete and mortar specimens using AE. In both concrete and mortar, three distinct stages of micro-cracking activity (initiation, stable growth and nucleation prior to the final failure) were distinguished. Verbruggen et al. [8] used both the digital image correlation (DIC) technique and acoustic emission for continuous monitoring of hybrid composite-concrete beams during loading in four-point bending. Lacidogna et al. [9,10] applied acoustic emission and dynamic identification techniques to examine damage progression in pre-notched concrete beams tested in four-point bending. They observed a decrease in the natural bending frequencies with the increase of the stored AE energy. The failure process of self-compacting concrete under compression was observed by Niewiadomski and Hoła [11]. They studied the influence of nanoparticles on acoustic emission parameters. Logoń and Schabowicz [12] used the AE technique to identify microcrack events in concrete beams reinforced with polypropylene fibres. They concluded that the analysis of the spectra provides an indicator of the destruction process. The characterisation of failure mechanisms of carbon nanotubes and graphene nanoplatelets-cement composites was investigated by Xu et al. [13] and Ashraf et al. [14]. They found that it was possible to differentiate the cracking pattern between micro and macro-cracks based on the AE parameters.

The above-reported works and many others proved the effectiveness of the acoustic emission method in the evaluation of concrete structures. Nevertheless, the precise indication of the moment of formation of micro-cracks remains a challenge, despite the fact that some mechanical energy is emitted when local load drops are recorded [15,16]. Moreover, most of the reported works concern experimental investigations. Only a limited number of studies have been devoted to both numerical and experimental studies of the interaction of elastic waves with developed micro-crack zones. An attempt to use a discontinuum model to simulate rock behaviour was undertaken by Hazzard and Young [17]. The 2D bonded-particle model was used to simulate a compressive failure test on a granite sample model with simultaneous recording of AE signals. Zhu et al. [18] performed numerical simulations of the AE activity during the failure process. They considered the concrete as a heterogeneous material using the finite element method. Each of the phases of the concrete (the cement matrix phase, the aggregate phase and the matrix-aggregate interface phase) was modelled separately using mesoscopic scale four-node isoparametric finite elements. Ji and Di [19] applied simplified discrete element modelling (DEM) of acoustic emission features in the fracture of rocks. They applied spherical particles bonded via the parallel bond model. Lisjak et al. [20] described a method dedicated to AE modelling based on the combined finite-discrete element method. Four-node cohesive elements (i.e. crack elements) simulated the development of fracture process zones (FPZs). Iturrioz et al. [21] carried out experimental studies of fracture monitoring in concrete specimens based on AE and supplemented them by numerical modelling using a simple truss-like discrete element method. Chong et al. [22] numerically simulated the acoustic emission characteristics of a jointed rock mass. First, the parallel bond model was prepared and then an additional sub-program was used to obtain the magnitude of the AE events by calculating the moment tensor. The comprehensive numerical and experimental study on the failure analysis of porous concrete was presented by Xie et al. [23]. The investigations were carried out on a specimen composed of the 10–25 mm aggregate bonded with cement mortar. The AE events were registered in experiments. The numerical model consisted of aggregate particles and linear parallel bonding between them. From the model, the number of cracks formed during the compression of the porous concrete sample was counted and compared with the AE energy cumulative curve. Zhang et al. [24] described compression tests on coal specimens monitored by the AE method. A numerical simulation of the cracking behaviour was performed by the discrete element method, using the particle flow code with the linear parallel bond model. The crack amount during biaxial compressive loading was calculated and compared with the cumulative AE counts registered during the experiments. Cheng et al. [25] carried out an acoustic emission simulation of cemented tailings backfill. They used particle flow code and compared the relationship between the number of microcracks from simulations and the magnitude of AE events from experiments. Zhu et al. [26] employed a local crack opening displacement softening model, in the framework of the discrete element method, to analyse the fracture behaviour of concrete bending beams. The numerically obtained failure patterns were compared with experimental results from AE and DIC techniques.

Recently, heterogeneous models of civil engineering materials have attracted the interest of researchers investigating various aspects of wave propagation-based damage detection methods (e.g. [27,28,29,30,31,32,33,34]). Such numerical models are extremely important to explore in order to enhance the interpretation of results of non-invasive diagnostics. To the best of the authors' knowledge, there is a lack of an accurate numerical model capable of capturing the transient elastic waves generated as a result of concrete fracture.

This study presents comprehensive coupled experimental–numerical analyses of concrete beams under three-point bending. The research is focused on the monitoring of micro-cracks evolution using the acoustic emission technique. The main objective of this paper is to explore the mechanism behind the generation of elastic waves during acoustic emission events and their interaction with micro- and macro-cracking in concrete structures under monotonic quasi-static loading. This aim was realized by developing a DEM model and numerical modelling of AE effects. An improved 4-phase DEM model, consisting of aggregate, mortar, macro-pores and porous

ITZs, is applied to analyse AE events in concrete. The main advantage is that the model is based on real mesostructured samples obtained directly from the laboratory as the identical size, position, and shape of the aggregates are crucial for studying elastic wave propagation. Additionally, the model can simulate aggregate breakage, which significantly influences the final results. Special attention was given to the propagation of elastic waves, which were registered during both the laboratory experiments and the numerical calculations. The developed DEM model was successfully applied to monitor the initiation, development, and propagation of cracks using the acoustic emission technique. In future research, the utilization of DEM models can potentially complement laboratory tests, leading to more comprehensive numerical investigations that can improve future applications of the AE technique (e.g. sensor localization).

2. Experimental investigations on bending beams

2.1. Specimens

The specimens used in this study were made from the same concrete mix, with the following components: cement CEM I 42.5R (330 kg/m^3), aggregate 0/2 mm (710 kg/m^3), aggregate 2/8 mm (664 kg/m^3), aggregate 8/16 mm (500 kg/m^3), water (165 kg/m^3) and super-plasticizer (0.7 % of the cement content). Concrete prisms were first produced and then 40 × 40 × 160 mm^3 beam specimens were cut from them. The beams had notches with a width of 4 mm and a depth of 7 mm, in the middle of the span. The experiments and simulations described in this paper were conducted on three beams, designated as #1, #2 and #3 (see Fig. 1).

Fig. 1. The tested concrete specimens: (a) beam #1, (b) beam #2 and (c) beam #3.

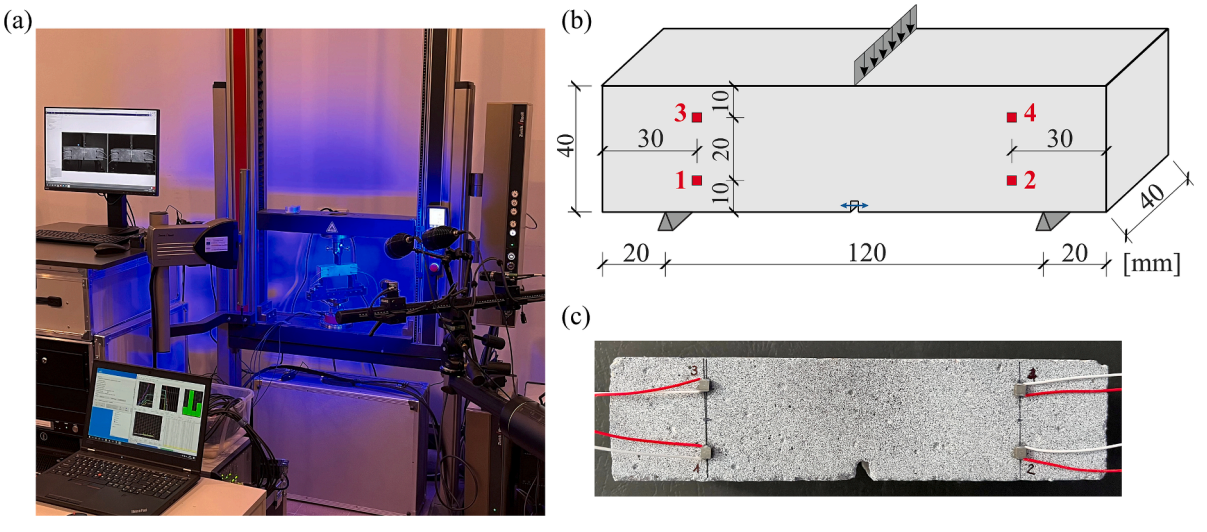

Fig. 2. Experimental setup (a) scheme of location of PZT sensors and configuration during bending test (b) and (c) front view on a beam with PZT sensors.

2.2. Experimental setup and procedure

The fracture process of concrete beams was investigated in a 3-point bending test, with a support spacing of 120 mm. The experimental setup is shown in Fig. 2a. Bending was performed on a Zwick Z10 universal testing machine (UTM), with a constant displacement rate of 0.05 mm/min. A preload of 20 N was applied at the start. The bending test was then carried out to a displacement of 0.3 mm, so that the total duration of the test was 360 s.

Acoustic emission (AE) and digital image correlation (DIC) techniques were used to characterise crack evolution during the bending process. Acoustic emission signals were recorded using the Vallen AE system with a threshold of 30.1 dB and a sampling rate of 10 MHz. Four multilayer piezoelectric transducers (Noliac NAC2024) were used for wave sensing. The arrangement of the sensors (numbered from S1 to S4) is shown in Fig. 2b and 2c. Simultaneously with the AE measurements, images of the front side of the beams were taken with a sampling frequency of 1 Hz.

3. DEM modelling

3.1. Formulation of DEM for concrete

In this study, the discrete element method (DEM) was chosen for the numerical calculations. The open-source code Yade ([35,36]) was used. In general, DEM is a perfect tool for modelling crack initiation and growth because it allows separate elements to be taken into account. In DEM models, the material is composed of particles that interact with each other during transitional and rotational motion, through a contact law and Newton's 2nd law via an explicit time-stepping scheme [37]. For concrete modelling, the main advantage is that discontinuities caused by fracture or fragmentation can be easily represented. The ease of access to information at the particle scale makes DEM a handy tool for studying the dynamics of systems composed of particles. The direct geometry, based on the experimental one, can be easily modelled with the exact size, shape and position of the aggregates.

In our model, the linear normal contact under compression has been assumed. Note, that there is no softening in the law (the global softening results directly from the geometry of the specimen). The cohesive bond was introduced to mimic brittle failure under the critical normal tensile force. Failure in the tangential direction causes initiated contact slip and sliding obeying the Coulomb friction law. The normal and tangential laws are presented in Fig. 3. The following equations can briefly describe the model:

$$\boldsymbol{F}_n = K_n(U - U_0)\boldsymbol{N}, \qquad \boldsymbol{F}_s = \boldsymbol{F}_{s,prev} + K_s \Delta \boldsymbol{X}_s \tag{1}$$

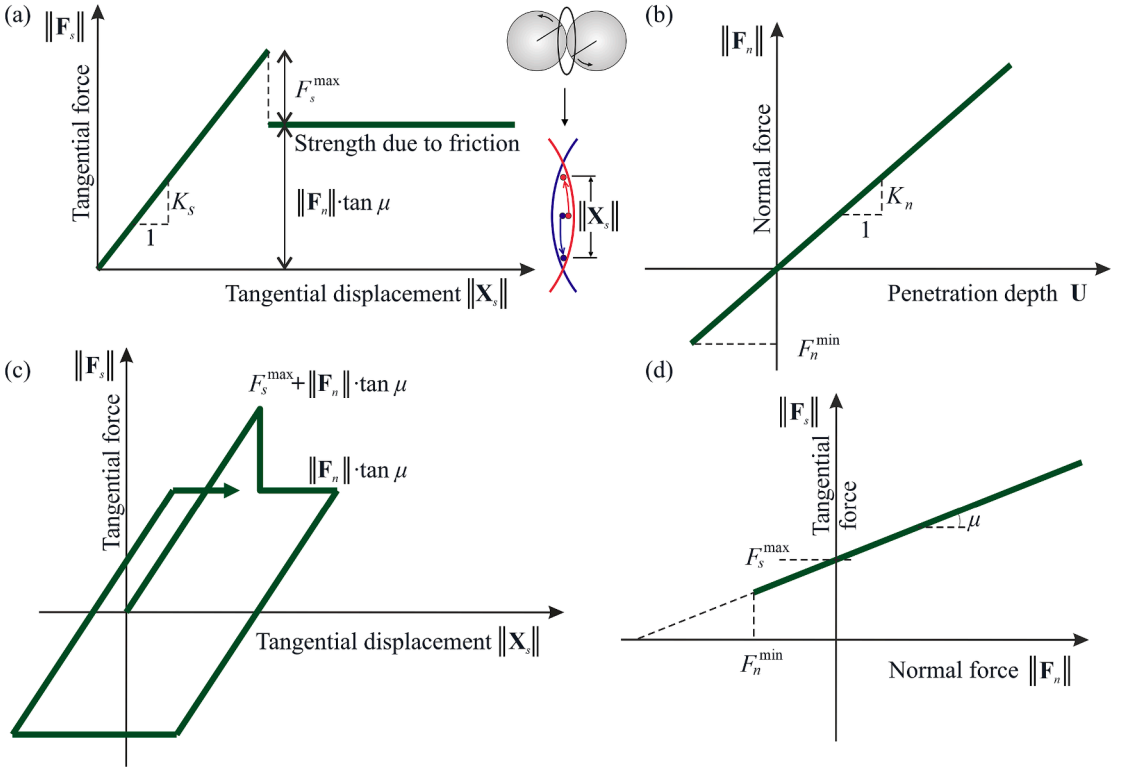

Fig. 3. Mechanical response of DEM: a) tangential contact model, b) normal contact model, c) loading and unloading path in tangential contact model and d) modified Mohr-Coulomb model (redrawn after [35,36]).

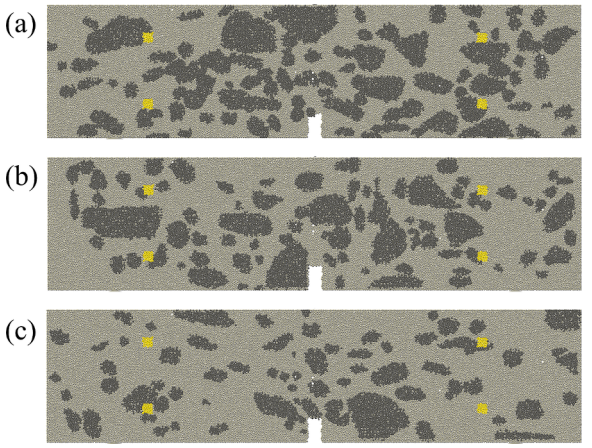

Fig. 4. Numerical DEM models for experimentally investigated concrete specimens: (a) beam #1, (b) beam #2 and (c) beam #3.

where $\boldsymbol{F}_n$ and $\boldsymbol{F}_s$ are the normal and tangential forces acting on the element, K_n and K_s are the normal and tangential stiffness of the contact, U and U_0 are the current and initial overlap between elements, $\boldsymbol{N}$ is a normal vector laying on the line between centres of the elements, $\Delta\boldsymbol{X}_s$ is the increment of the relative tangential displacement and $\boldsymbol{F}_{s,prev}$ is the tangential force from the previous iteration. Note, that during the test, the initial overlap U_0 is extracted from the current one. This is an own modification to be able to create very dense samples (even with 1 % of porosity), which is not possible in common DEM codes. This improvement is very important for concrete calculations where the porosity is around 5 %.

The normal and tangential stiffness can be calculated from a linear law depending on the radii of the elements:

$$K_n = E_{DEM}\frac{2R_AR_B}{R_A+R_B}, \qquad K_s = \nu_{DEM}E_{DEM}\frac{2R_AR_B}{R_A+R_B} \tag{2}$$

where E_{DEM} is a material stiffness at the microscale and ν_{DEM} is a normal to tangential stiffness ratio (sometimes called the Poisson's ratio of contact). R_A and R_B are the radii of elements in contact. It is important to note here, that E_{DEM} and ν_{DEM} are the micro parameters, and must be calibrated to obtain the correct global stiffness and Poisson's ratio for the whole specimen.

The tangential law follows the Coulomb friction law. It has a form depending on the stage of the contact, i.e. before the contact is broken, it is described by the equation

$$\|\boldsymbol{F}_s\| - F_s^{\max} - \|\boldsymbol{F}_n\| \cdot \tan\mu \leqslant 0 \tag{3}$$

while after the contact is broken it has the form:

$$\|\boldsymbol{F}_s\| - \|\boldsymbol{F}_n\| \cdot \tan\mu \leqslant 0 \tag{4}$$

where μ is the intergranular friction angle.

Finally, the limit for the bond can be calculated as:

$$F_s^{\max} = CR^2, \qquad F_n^{\min} = TR^2 \tag{5}$$

where $F_s^{\max}$ and $F_n^{\min}$ are the critical cohesive and maximum tensile forces, respectively; C is the maximum shear stress at zero pressure; T is the maximum normal tensile stress; R is the radius of the smaller element in the contact. The crack (fracture) is obtained because one of the above equations is satisfied. Since cohesion is broken (whether in the normal or tangential direction), the bond does not reappear in the remaining test. The choice of a very simple constitutive law was intended to capture, on average, different contact possibilities in real concrete. Further details of the model can be found in [38 39].

3.2. Numerical model of concrete beam

In this paper, the calculations have been limited to 2D. The 3D analysis is more realistic than the 2D one [40], however, the 2D calculations can also be useful as a means of studying several different relationships [41]. The main advantage of 2D calculations is time-saving. The concrete material was described as 4-phase with aggregate, surrounding interfacial transition zones (ITZs), mortar and air voids. The specimen size was the same as in the experiment (except for the width): length 80 mm and height 40 mm with a notch in the centre (4×7 mm^2). The position, size and shape of the aggregates were taken directly from the photographs of the laboratory samples. The aggregates were modelled as an assembly of small elements connected by linear law. It is worth noting that in previous studies, the aggregates were modelled as rigid clusters. The refinement, used in this paper, allows for aggregate breakage, which is an important issue in concrete analysis, particularly in the simulation of AE events. The elements within the aggregate had a

Table 1
DEM parameters used in numerical simulations.

Parameter	Mortar	ITZ	Aggregate
E_{DEM} [GPa]	27.42	19.19 (70 %)	109.68 (400 %)
$\nu_{DEM}(K_n/K_s)$ [-]	0.17	0.17	0.17
μ [°]	18	18	18
T [MPa]	24.23	16.96 (70 %)	96.92 (400 %)
C [MPa]	48.46	33.92 (70 %)	193.84 (400 %)

radius between 0.177 mm and 0.329 mm. This was chosen to model the aggregate shape with high accuracy. The same range of element sizes was used to mimic the mortar between the aggregates. The initial porosity was equal to 5 %, as in the experiment. The ITZs were assumed to be a contact between aggregate and mortar elements, so they had no physical width, contrary to [42]. This assumption has a negligible effect on the results but greatly reduces the computation time. The macroscopic air voids were modelled as empty spaces. The final number of elements was approximately 31 000. The geometries are shown in Fig. 4. Light grey indicates mortar, dark grey is aggregate, and yellow spots are PZT sensor positions.

For the discrete element method, the six main parameters are required: ρ, E_{DEM}, υ_{DEM}, μ, C and T. The density ρ was chosen as 2500 kg/m^3, to correspond to the real weight of the laboratory sample, i.e. the sample in DEM in 3D with the same porosity weighed the same as the experimental beam. The 5 remaining parameters were calibrated by trial-and-error method to obtain a macroscopic behaviour compatible with the experiment. Note, that the calibration was performed on a uniaxial compression test in the 3D model, without the real shape of the aggregates. The bending beam tests have just been validated. The mortar-aggregate contacts (ITZs) were reduced by 30 % compared to the mortar-mortar contacts, as this is the weakest phase in ordinary concrete (both in terms of strength and stiffness). This value was based on nanoindentation studies by Xiao et al. [43], Xie et al. [44] as well as Nitka and Tejchman [42]. It was also verified in previous numerical calculations [41,42] as the most appropriate value by comparison with the real fracture (crack shape). The contact within the aggregate was increased by a factor of 4 [42]. The final parameters for each phase used in this study are summarised in Table 1.

During the bending test in the DEM model, a constant vertical velocity of 0.5 mm/s was applied to the piston. The so-called inertial number I was kept below 10^{-4}, to ensure the quasi-static conditions [45]. The displacement of the piston and the CMOD (crack mouth opening displacement) were measured throughout the test. At the same time, the number of broken contacts was tracked. As in the experiment, four areas of interest were modelled to mimic multilayer piezoelectric transducers. The sensors in the numerical model were positioned in the same locations as in the laboratory tests, as depicted in Fig. 2. In these specific regions, the average velocities of the elements were computed, considering the velocities as the primary component of the elastic wave. The numerical DEM results obtained were carefully compared with the experimental data in the following section to ensure a thorough analysis of the results.

4. Results and discussion

4.1. Bending test

Fig. 5a shows the load–deflection and load-CMOD curves for all the beams tested. The load–deflection curves were obtained directly from the testing machine, while the load-CMOD curves were obtained based on DIC measurements, using the virtual extensometer of 10 mm length located in the notch area (cf. Fig. 2b). The corresponding numerical curves, obtained from DEM calculations, are presented in Fig. 5b. The load–deflection curves for all specimens tested were similar in shape in a pre-peak region and tended to follow an almost linear trend. They decreased sharply and showed a brittle failure after reaching the maximum bending strength.

The experimental peak load values were: 1784.29 N, 1764.93 N, and 1897.96 N, for specimens #1, #2 and #3 respectively. The mean value was 1815.73 N, the standard deviation (SD) was 71.87 N and the coefficient of variation (COV) was 3.96 %. The numerical peak load values were: 2018.31 N, 1799.95 N, and 1846.32 N, for specimens #1, #2 and #3 respectively. The mean value was 1888.19 N, the standard deviation (SD) was 115.04 N and the coefficient of variation (COV) was 6.09 %.

The peak in the numerical calculations is slightly earlier in the load–displacement curve, but the maximum force has a similar value. In the load-CMOD curve, the DEM calculations show higher brittleness than the experimental data. This is due to the 2D calculations, as the 3D model shows higher ductility [40]. In addition, 2D simulations cause large fluctuations during the test (see disturbances of curves in Fig. 5b), as a broken contact significantly affects the global response (due to an insufficient number of initial contacts). However, the global trend can be captured from DEM simulations, and it is similar to experiments.

Fig. 6 shows the fracture maps of the tested beams obtained from both experimental and numerical investigations. The first column shows maps obtained from DIC measurements. The horizontal strain components were determined at a crosshead displacement of 0.3 mm. The second column shows photographs of the beams taken at the end of the bending process. After the test, the specimens were washed to remove the speckle pattern and to observe the evolution of the cracks in relation to the aggregate grains. Finally, the numerical cracks are shown in the third column. The elements that lost contact are coloured. The blue colour corresponds to the lack of contact within the mortar phase, and the purple colour corresponds to the grain breakage. The yellow colour indicates damage within the ITZs. The macro crack (white space) has been magnified 10 times, for better visualisation. The shape of the numerical crack was similar to that of the experimental crack. There were some differences such as a broken upper aggregate in the DEM model for beam #2

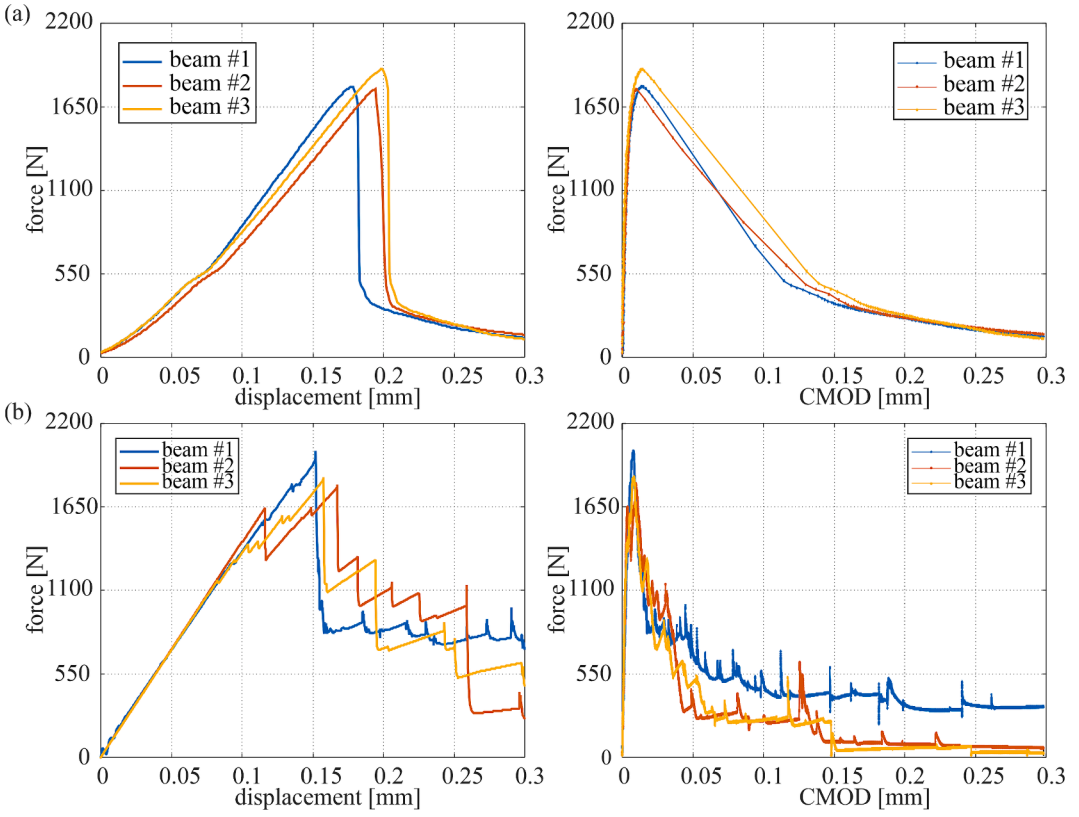

Fig. 5. Load-displacement and load-CMOD curves for beams #1 – #3: (a) experimental; (b) numerical.

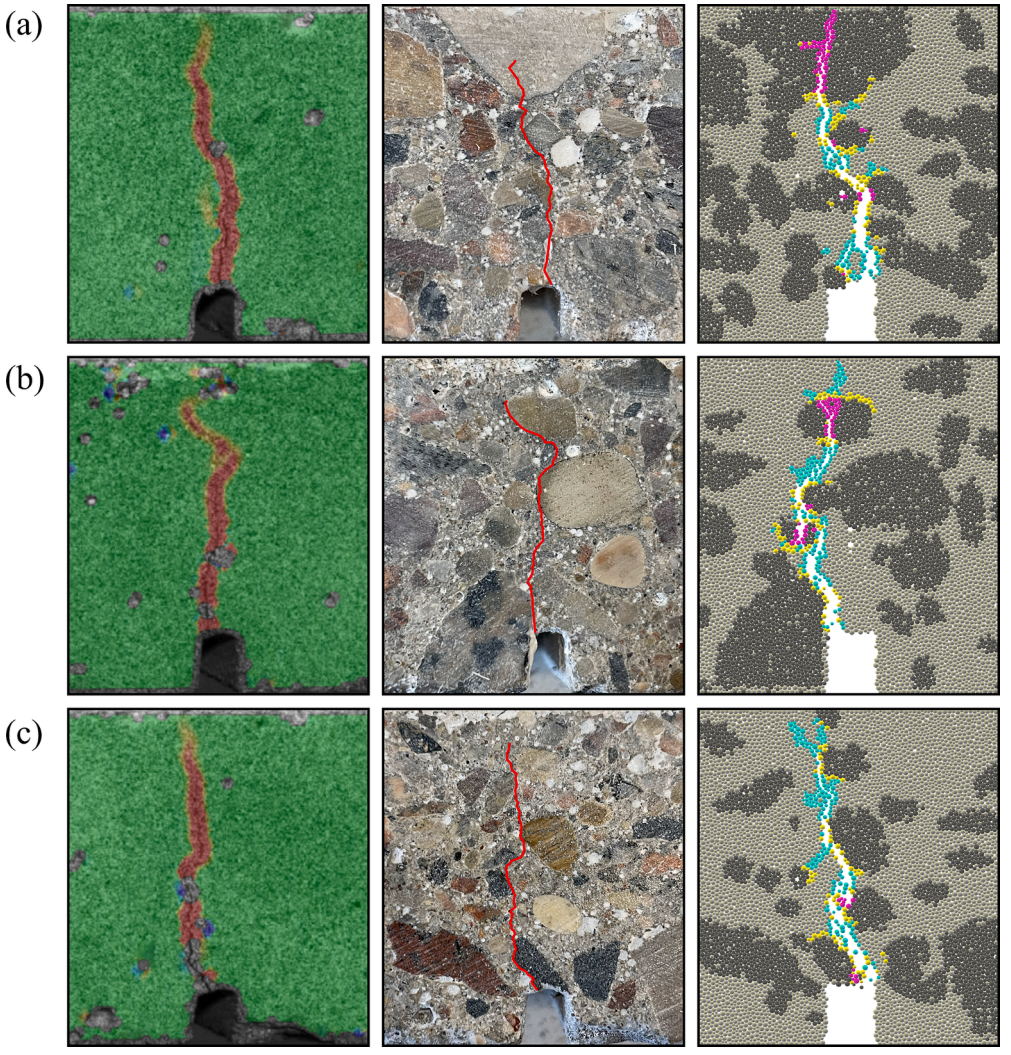

Fig. 6. Fracture in investigated specimens: (a) beam #1, (b) beam #2 and (c) beam #3 (in DEM models the colours denote broken contact in the mortar (blue), aggregate (pink) and ITZ (yellow) phase). (For interpretation of the references to colour in this figure legend, the reader is referred to the web version of this article.)

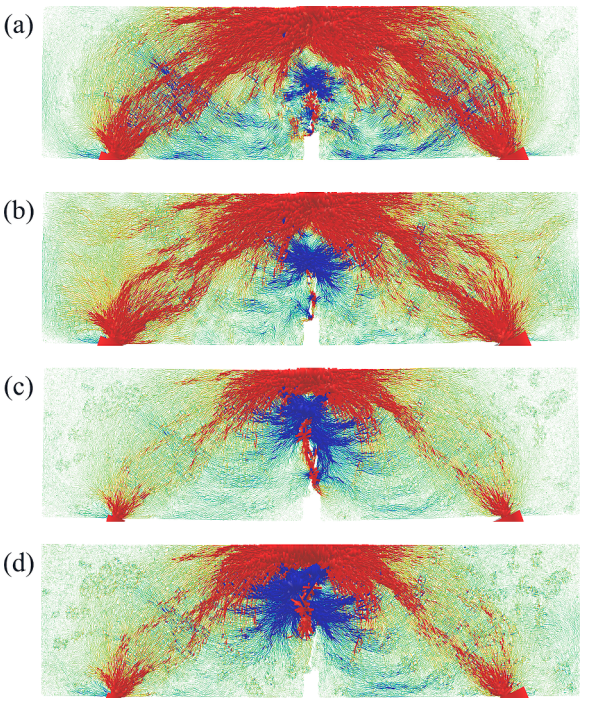

Fig. 7. Distribution of forces in DEM model of beam #1, for different values of CMOD: (a) 0.008 mm, (b) 0.011 mm, (c) 0.02 mm, (d) 0.03 mm (red – compression, blue – tension). (For interpretation of the references to colour in this figure legend, the reader is referred to the web version of this article.)

or a crack initiated on the opposite side of the notch in beam #3. This was due to the 2D calculations not taking depth into account.

In Fig. 7, the evolution of the internal normal forces for beam #1 is shown. For the other beams calculated, the distribution of forces was similar. The red and blue colours show strong force chains in compression and tension modes, respectively. The green colour indicates weak forces. The strong compression forces were located between the supports and the piston with the higher values just below the piston which is typical of the bending test. The main tension region was located in the middle-bottom part of the beam. As the crack started to develop, the tensile region moved upwards, just at the crack tip. Strong compressive forces were observed on both sides of the crack, due to interlocking.

4.2. AE results

In this section, the fracture process of concrete specimens has been comprehensively analysed using experimental and numerical data. In both measurements and numerical simulations, acoustic emission signals were first recorded and then processed to obtain energy values.

In Fig. 8, the evolution of the velocity field is presented. The blue colour indicates the velocity of a single sphere higher than an arbitrarily chosen value (for visualisation purposes). Initially, the higher velocity was obtained only in several elements close to the piston (Fig. 8a). When some contact was broken, a crack began to develop and the strong acceleration of elements close to the notch was observed (Fig. 8b,c). The wave propagated through the entire specimen and slowly decayed (Fig. 8d). The velocities were captured and registered at the location of the PZT sensors and analysed further.

The results in the form of cumulative energy plots for the experimental and numerical calculations are depicted in Fig. 9. In addition, load–displacement and load-CMOD curves have been included in this figure to give a more accurate representation of the bending process. For clarity and comparison between experimental and numerical values, the energy results shown have been normalised to unity.

Firstly, it is important to highlight the compatibility of the force–deflection and force-CMOD curves obtained for the experimental and numerical data. The analysis of the energy results obtained also shows similarities for all the beams tested. It can be seen, that the cumulative energy curves characterise the force–deflection behaviour. In the case of the experimental data, the first small increase in energy occurred before the maximum force was reached. The start of the increase corresponded to a noticeable change in the slope of the force–deflection curve and possible small interactions between the beam and flexure fixture. The sudden increase occurred at the peak load value. The subsequent increases in AE activity in the post-peak phase were related to the gradual development of the crack. The sudden, single jump in cumulative energy observed in beam #1 (at about 0.28 mm deflection) could be related to the breakage of the aggregate located in the upper part of the beam, see Fig. 6, as aggregate fracture can induce high energy emission events. In beams #2 and #3, the cracks omitted the aggregates (on the surface inspected), so that several smaller energy jumps occurred in the post-peak

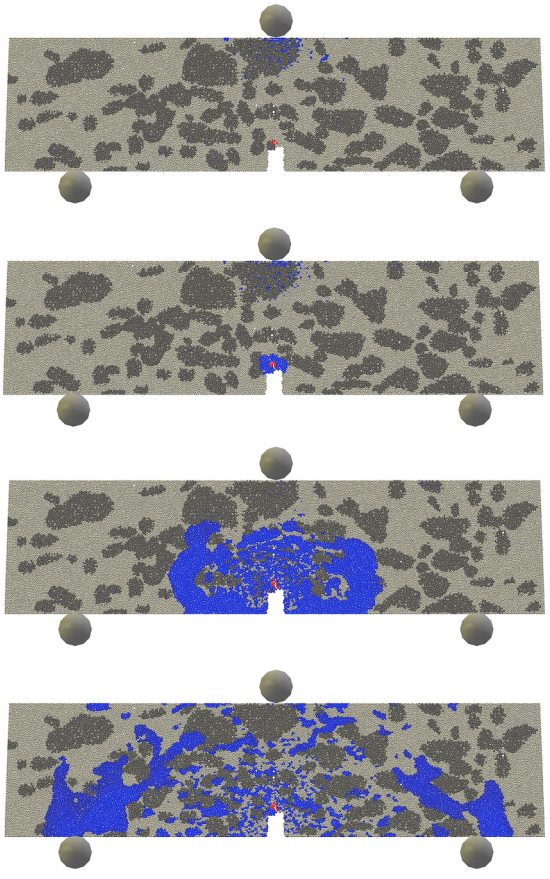

Fig. 8. Snapshots of velocity fields in the DEM model of beam #1, between CMOD of 0.004–0.005 mm (when the first crack appeared).

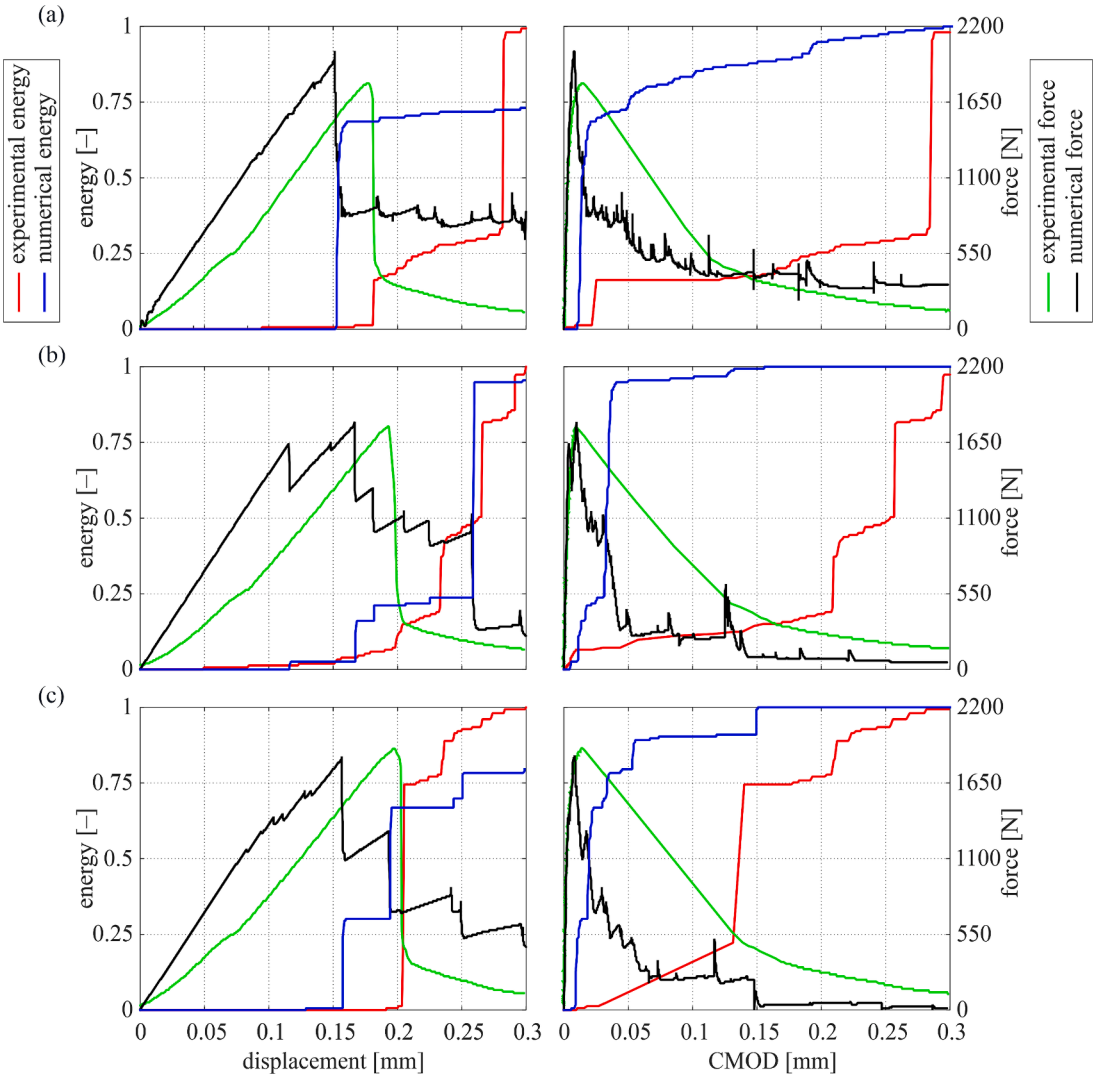

Fig. 9. AE analysis results: cumulative energy-displacement/CMOD for experimental and numerical data: (a) beam #1, (b) beam #2, (c) beam #3.

phase, corresponding to the formation of macro-cracks, as a result of local snap-back phenomena (cf. [15]). In the numerical results, the first increments appeared when the maximum force was reached, and the subsequent increments had a more gradual character. This behaviour demonstrated the general correctness and accuracy of the DEM calculations performed. In the plots on the right side of Fig. 9, in the CMOD domain, the effect of the expanding crack on the energy changes can be observed. For both the experimental and numerical results, the first significant increase in cumulative energy occurred at the point of maximum force onset and immediately after. This behaviour was related to the sudden increase in the size of the resulting crack. After this phenomenon, the energy gradually increased and stabilised until the end of the test.

Figs. 10 and 11 present the cumulative energy for each sensor separately, as a function of the displacement of the cross-head and CMOD, respectively. The experimental results are given on the left and the numerical ones on the right side. The difference in the energy value recorded by different sensors is due to the evolution and direction of the crack. The sensor that received the signal in the shortest time indicated a higher energy value. When analysing the experimental plots, it is noticeable that in the initial phase the energy is at a similar level for all sensors. Before the maximum force was reached, i.e. when micro-cracks were formed, more energy was recorded by sensors 1 and 2, located at the bottom of the beam. In the later loading phase of the load, larger increments were recorded by the upper sensors as the crack propagated. It can also be seen that sensors 1 and 3 recorded more energy in beams #1 and #3 as the crack turned in their direction. Slightly different behaviour can be seen in the energy diagrams obtained from DEM calculations. After first dropping of the force, largest values of the energy were recorded by sensors 1 and 2, located at the bottom of the beam. This trend was maintained until the end of the bending test. It can be concluded that due to the 2D calculations, the influence of the place of beginning of the crack was greater then their further direction of the development.

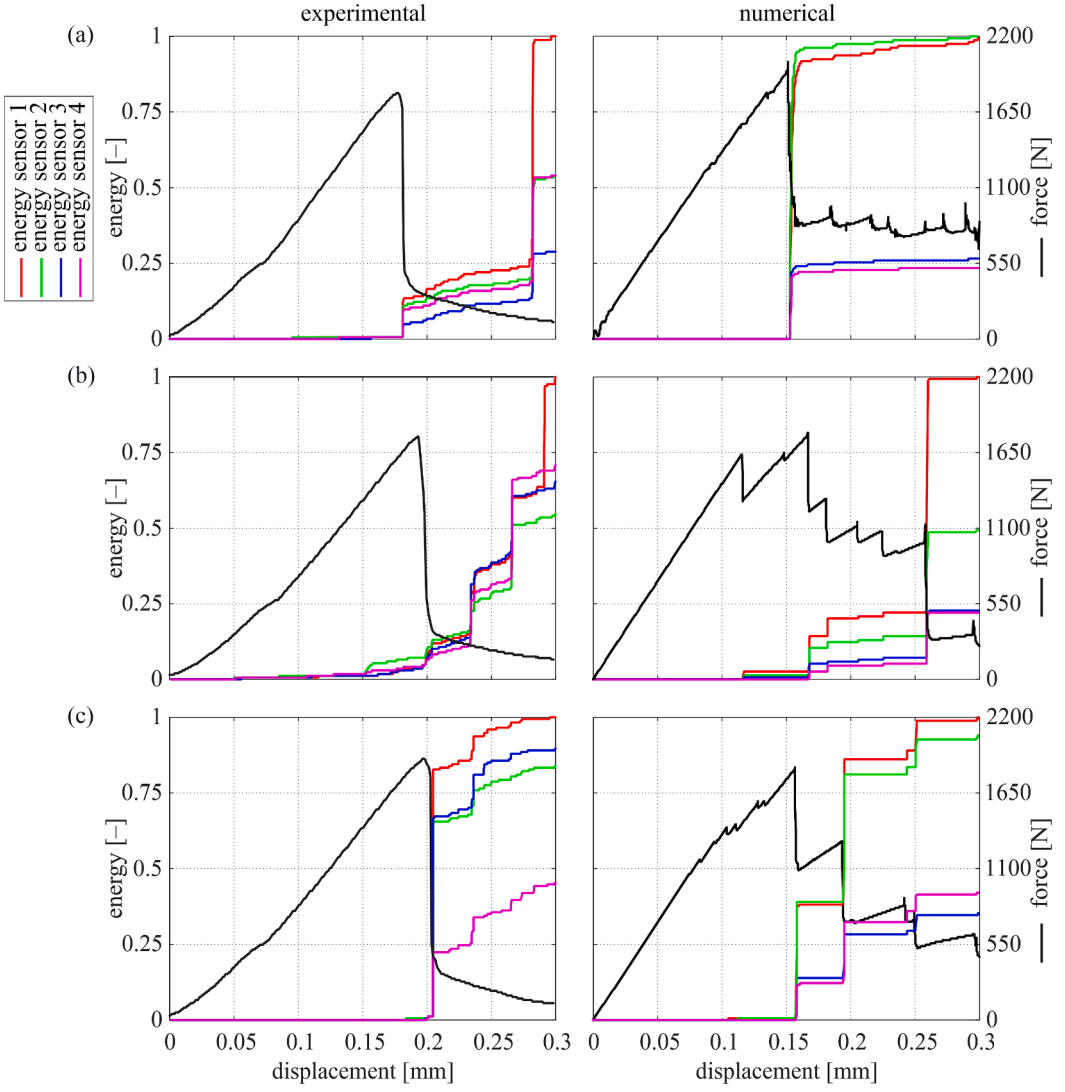

Fig. 10. AE analysis results for particular sensors: cumulative energy-displacement for experimental and numerical data: (a) beam #1, (b) beam #2, (c) beam #3.

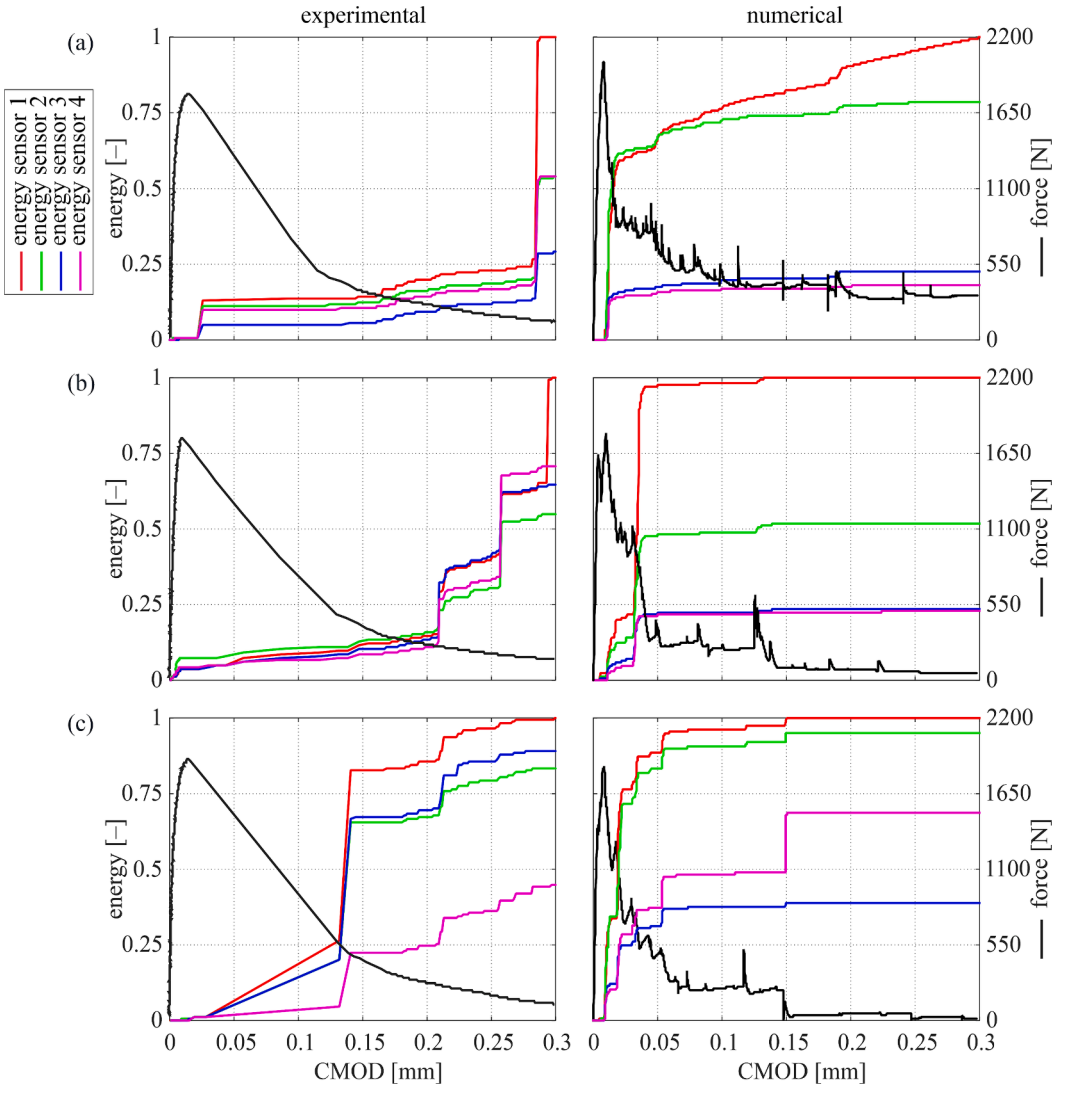

Fig. 11. AE analysis results for particular sensors: cumulative energy-CMOD for experimental and numerical data: (a) beam #1, (b) beam #2, (c) beam #3.

Fig. 12 presents the results of the AE analysis and crack evolution for the numerical DEM calculations. The force/energy-CMOD curves are shown in the CMOD range from 0 to 0.03 mm. This allowed the crack evolution to be highlighted in the early stages. Six points for different values of CMOD were selected, to compare the behaviour of the force and energy changes with the crack

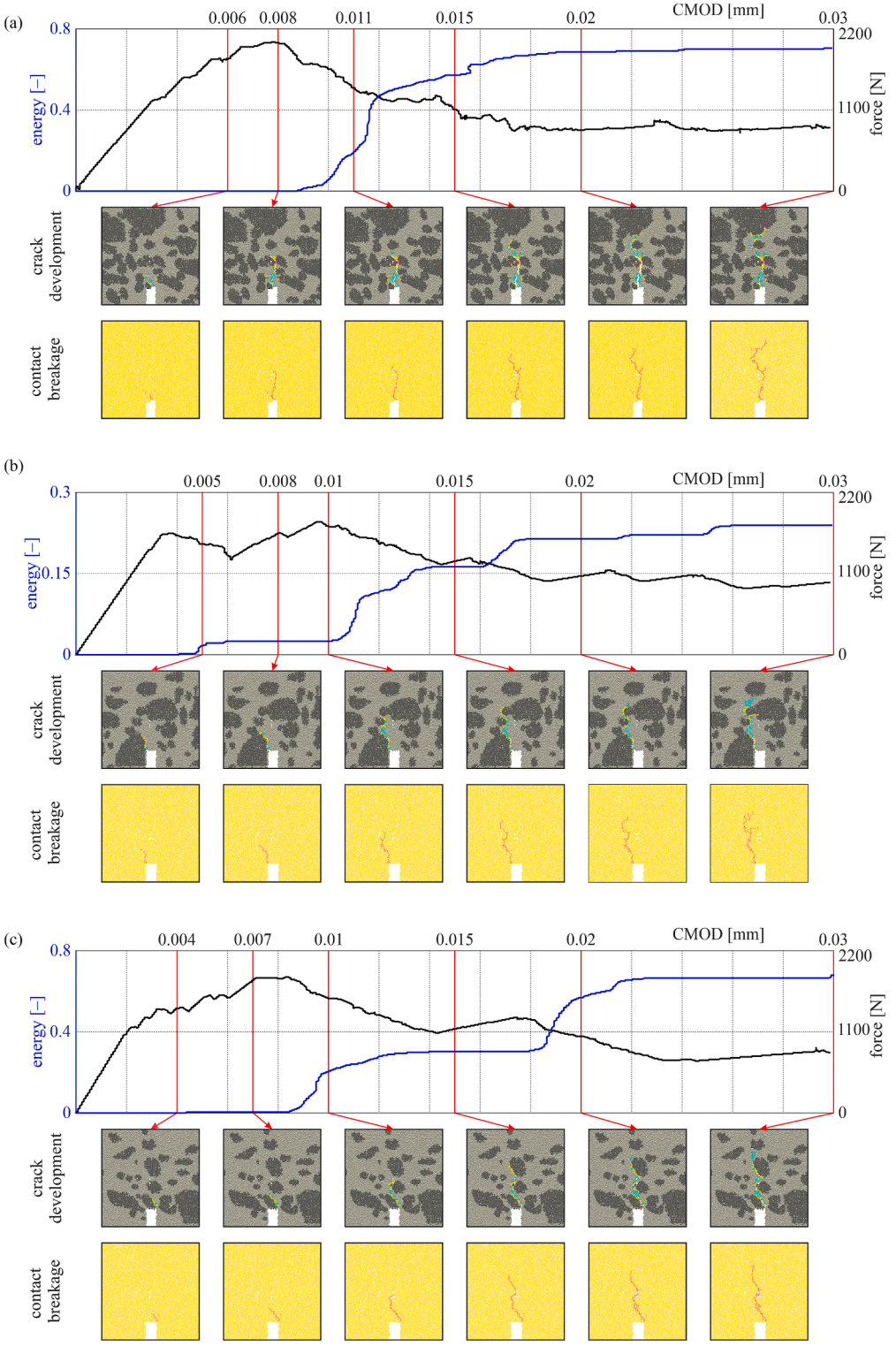

Fig. 12. AE numerical results: cumulative energy–CMOD, crack development and contact breakage: (a) beam #1; (b) beam #2; (c) beam #3.

evolution. At each of these points, maps of crack development and contact breakage are shown. It can be noted that with the initiation of the crack, the registration of energy growth began, and some changes in the force curve occurred. Each loss of contact resulted in a fluctuation of the force curve and some increase in cumulative energy, with a slight shift in time. The main increase in energy occurred just after the peak force was reached, due to fracture.

5. Conclusions

This paper investigated the monitoring of the fracture process of concrete beams subjected to bending. The use of two non-destructive techniques, namely acoustic emission and digital image correlation provided important insights into the internal state of the specimens throughout the three-point bending test. Digital image correlation allowed the crack propagation to be observed, while the acoustic emission method allowed the fracture process to be monitored. To investigate the feasibility of numerical modelling of AE effects, the experiment was simulated using DEM.

The DEM calculations exhibited good agreement at both the micro and macro levels. The global strength and stiffness of the specimen were found to be comparable, although with slightly reduced ductility as a result of the 2D calculations. The resulting numerical crack shape was very similar to the real counterpart, as the actual geometry of the DEM model was taken directly from the laboratory specimen. The DEM model proved to be a valuable tool for concrete damage calculations. The experimental and numerical results demonstrated consistency and alignment with each other.

Furthermore, the performed numerical calculations facilitated the analysis of acoustic emission. The signals recorded by numerical sensors were successfully processed to obtain variations in energy throughout the bending test. Changes and jumps at the force curve caused by micro-cracks corresponded to changes in the energy of AE events. Any loss of contact (micro-crack) produced an elastic wave that could be registered by the sensors. It is worth noting that these results were also in good agreement with the experimental data. In the experiments, a higher value was found on the bottom sensors at the beginning of the test, while later, the upper sensors were more active. In contrast, in the numerical calculations, only the bottom sensors were dominant during the whole test. In DEM, the first crack produced the most energy, and the developing crack had a less significant effect.

This research takes the initial step towards explaining the mechanism of elastic waves emitted in AE events and their interaction with micro- and macro-cracking in concrete elements subjected to monotonic quasi-static loading. This knowledge is essential for the detection of cracks in concrete at an early stage of deformation. In future studies, a precise 3D model will be examined to accurately capture the phenomena of the elastic wave in heterogeneous material. Also, the influence of the aggregate shape and macro pores will be examined in detail.

CRediT authorship contribution statement

Magdalena Rucka: Conceptualization, Methodology, Investigation, Formal analysis, Writing – original draft, Writing – review & editing, Supervision, Project administration, Funding acquisition. **Magdalena Knak:** Conceptualization, Methodology, Investigation, Formal analysis, Visualization, Writing – original draft. **Michał Nitka:** Conceptualization, Methodology, Investigation, Formal analysis, Visualization, Writing – original draft, Writing – review & editing.

Declaration of Competing Interest

The authors declare that they have no known competing financial interests or personal relationships that could have appeared to influence the work reported in this paper.

Data availability

Data will be made available on request.

Acknowledgements

The study was financed by the National Science Centre, Poland, under the project “Complex investigations of the development of micro- and macro-cracks in concrete members using elastic waves: experiments and discrete element method modelling” no 2019/35/B/ST8/01905.

References

[1] Accornero F, Cafarelli R, Carpinteri A. The cohesive/overlapping crack model for plain and RC beams: Scale effects on cracking and crushing failures. Mag. Concr. Res. 2022;74:433–50. https://doi.org/10.1680/jmacr.20.00260.
[2] Carpinteri A, Accornero F. Dimensional Analysis of Critical Phenomena: Self-Weight Failure, Turbulence, Resonance, Fracture. Phys. Mesomech. 2021;24:459–63. https://doi.org/10.1134/S102995992104010X.
[3] Kumar B, Ray S. A multi-scale based fracture characterization in concrete under fatigue loading using critical energy dissipation. Int. J. Fatigue 2022;165:107165. https://doi.org/10.1016/j.ijfatigue.2022.107165.
[4] Katsaga T, Sherwood EG, Collins MP, Young RP. Acoustic emission imaging of shear failure in large reinforced concrete structures. Int. J. Fract. 2007;148:29–45. https://doi.org/10.1007/s10704-008-9174-x.

[5] Aggelis DG, Soulioti DV, Sapouridis N, Barkoula NM, Paipetis AS, Matikas TE. Acoustic emission characterization of the fracture process in fibre reinforced concrete. Constr. Build. Mater. 2011;25:4126–31. https://doi.org/10.1016/j.conbuildmat.2011.04.049.
[6] Aggelis DG. Classification of cracking mode in concrete by acoustic emission parameters. Mech. Res. Commun. 2011;38:153–7. https://doi.org/10.1016/j.mechrescom.2011.03.007.
[7] Vidya Sagar R, Prasad RV, Raghu Prasad BK, Rao MVMS. Microcracking and Fracture Process in Cement Mortar and Concrete: A Comparative Study Using Acoustic Emission Technique. Exp. Mech. 2013;53:1161–75. https://doi.org/10.1007/s11340-012-9708-z.
[8] Verbruggen S, De Sutter S, Iliopoulos S, Aggelis DG, Tysmans T. Experimental Structural Analysis of Hybrid Composite-Concrete Beams by Digital Image Correlation (DIC) and Acoustic Emission (AE). J. Nondestr. Eval. 2016;35:1–10. https://doi.org/10.1007/s10921-015-0321-9.
[9] Lacidogna G, Piana G, Carpinteri A. Acoustic Emission and Modal Frequency Variation in Concrete Specimens under Four-Point Bending. Appl. Sci. 2017;7:339. https://doi.org/10.3390/app7040339.
[10] Lacidogna G, Piana G, Accornero F, Carpinteri A. Multi-technique damage monitoring of concrete beams: Acoustic Emission, Digital Image Correlation, Dynamic Identification. Constr. Build. Mater. 2020;242:118114. https://doi.org/10.1016/j.conbuildmat.2020.118114.
[11] Niewiadomski P, Hoła J. Failure process of compressed self-compacting concrete modified with nanoparticles assessed by acoustic emission method. Autom. Constr. 2020;112. https://doi.org/10.1016/j.autcon.2020.103111.
[12] Logoń D, Schabowicz K. The recognition of the micro-events in cement composites and the identification of the destruction process using acoustic emission and sound spectrum. Materials (Basel) 2020;13:2988. https://doi.org/10.3390/ma13132988.
[13] Xu J, Ashraf S, S., khan,, X., Chen,, A., Akbar,, F., Farooq,. Micro-cracking pattern recognition of hybrid CNTs/GNPs cement pastes under three-point bending loading using acoustic emission technique. J Build Eng 2021;42. https://doi.org/10.1016/j.jobe.2021.102816.
[14] Ashraf S, Khan S, Oad VK. Microcracking monitoring and damage detection of graphene nanoplatelets-cement composites based on acoustic emission technology. Case Stud. Constr. Mater. 2023;18:e01844.
[15] Carpinteri A, Accornero F. Multiple snap-back instabilities in progressive microcracking coalescence. Engng. Fract. Mech. 2018;187:272–81. https://doi.org/10.1016/j.engfracmech.2017.11.034.
[16] Lacidogna G, Accornero F, Carpinteri A. Influence of snap-back instabilities on Acoustic Emission damage monitoring. Engng. Fract. Mech. 2019;210:3–12. https://doi.org/10.1016/j.engfracmech.2018.06.042.
[17] Hazzard J, Young R. Simulating acoustic emissions in bonded-particle models of rock. Int. J. Rock Mech. Min. Sci. 2000;37:867–72. https://doi.org/10.1016/S1365-1609(00)00017-4.
[18] Zhu WC, Zhao XD, Kang YM, Wei CH, Tian J. Numerical simulation on the acoustic emission activities of concrete. Mater. Struct. 2010;43:633–50. https://doi.org/10.1617/s11527-009-9517-8.
[19] Ji S, Di S. Discrete element modeling of acoustic emission in rock fracture. Theor. Appl. Mech. Lett. 2013;3:021009. https://doi.org/10.1063/2.1302109.
[20] Lisjak A, Liu Q, Zhao Q, Mahabadi OK, Grasselli G. Numerical simulation of acoustic emission in brittle rocks by two-dimensional finite-discrete element analysis. Geophys. J. Int. 2013;195:423–43. https://doi.org/10.1093/gji/ggt221.
[21] Iturrioz I, Lacidogna G, Carpinteri A. Acoustic emission detection in concrete specimens: Experimental analysis and lattice model simulations. Int. J. Damage Mech 2014;23:327–58. https://doi.org/10.1177/1056789513494232.
[22] Chong Z, Yao Q, Li X, Shivakumar K. Acoustic emission investigation on scale effect and anisotropy of jointed rock mass by the discrete element method. Arab. J. Geosci. 2020;13. https://doi.org/10.1007/s12517-020-05303-z.
[23] Xie C, Yuan L, Zhao M, Jia Y. Study on failure mechanism of porous concrete based on acoustic emission and discrete element method. Constr. Build. Mater. 2020;235:117409. https://doi.org/10.1016/j.conbuildmat.2019.117409.
[24] Zhang L, Ren T, Li X, Tan L. Acoustic emission, damage and cracking evolution of intact coal under compressive loads: Experimental and discrete element modelling. Engng. Fract. Mech. 2021;252:107690. https://doi.org/10.1016/j.engfracmech.2021.107690.
[25] Cheng A, Shu P, Deng D, Zhou C, Huang S, Ye Z. Microscopic acoustic emission simulation and fracture mechanism of cemented tailings backfill based on moment tensor theory. Constr. Build. Mater. 2021;308:125069. https://doi.org/10.1016/j.conbuildmat.2021.125069.
[26] Zhu R, Alam SY, Loukili A. Relevance of displacement softening model in discrete element method to investigate structural and grain size scaling effect. Theor. Appl. Fract. Mech. 2023;123:103706. https://doi.org/10.1016/j.tafmec.2022.103706.
[27] Rojek J, Madan N, Nosewicz S. Micro-Macro Relationships in the Simulation of Wave Propagation Phenomenon Using the Discrete Element Method. Materials (Basel) 2019;12:4241. https://doi.org/10.3390/ma12244241.
[28] Asadollahi A, Khazanovich L. Numerical investigation of the effect of heterogeneity on the attenuation of shear waves in concrete. Ultrasonics 2019;91:34–44. https://doi.org/10.1016/j.ultras.2018.07.011.
[29] Yu T, Chaix JF, Audibert L, Komatitsch D, Garnier V, Hénault JM. Simulations of ultrasonic wave propagation in concrete based on a two-dimensional numerical model validated analytically and experimentally. Ultrasonics 2019;92:21–34. https://doi.org/10.1016/j.ultras.2018.07.018.
[30] Lachowicz J, Rucka M. A novel heterogeneous model of concrete for numerical modelling of ground penetrating radar. Constr. Build. Mater. 2019;227:116703. https://doi.org/10.1016/j.conbuildmat.2019.116703.
[31] Kurpińska M, Ferenc T. Experimental and numerical investigation of mechanical properties of light weight concretes (LWCs) with various aggregates. Materials (Basel) 2020;13:1–16. https://doi.org/10.3390/MA13163474.
[32] Hu J, Ma T, Ma K, Xu J. Three-dimensional discrete element simulation on degradation of air voids in double-layer porous asphalt pavement under traffic loading. Constr. Build. Mater. 2021;313:125570. https://doi.org/10.1016/j.conbuildmat.2021.125570.
[33] Chen P, Liu J, Cui X, Si S. Mesoscale analysis of concrete under axial compression. Constr. Build. Mater. 2022;337:127580. https://doi.org/10.1016/j.conbuildmat.2022.127580.
[34] Avadh K, Jiradilok P, Bolander JE, Nagai K. 3D mesoscale simulation of the influence of corrosion on loss of tension stiffening in reinforced concrete. Constr. Build. Mater. 2022;339:127684. https://doi.org/10.1016/j.conbuildmat.2022.127684.
[35] Kozicki J, Donze FV. A new open-source software developer for numerical simulations using discrete modeling methods. Comput. Methods Appl. Mech. Engng. 2008;197:4429–43. https://doi.org/10.1016/j.cma.2008.05.023.
[36] V. Šmilauer, B. Chareyre, Yade DEM Formulation, in: Yade Doc., The Yade Project , 1st ed., 2010. http://yade-dem.org/doc/formulation.html.
[37] Cundall PA, Strack ODL. A discrete numerical model for granular assemblies. Geotechnique 1979;29:47–65.
[38] Nitka M, Tejchman J. Modelling of concrete behaviour in uniaxial compression and tension with DEM. Granul. Matter 2015;17:145–64. https://doi.org/10.1007/s10035-015-0546-4.
[39] Suchorzewski J, Nitka M. Size effect at aggregate level in microCT scans and DEM simulation – Splitting tensile test of concrete. Engng. Fract. Mech. 2022;264:108357. https://doi.org/10.1016/j.engfracmech.2022.108357.
[40] Nitka M, Tejchman J. A three-dimensional meso-scale approach to concrete fracture based on combined DEM with X-ray μCT images. Cem. Concr. Res. 2018;107:11–29. https://doi.org/10.1016/j.cemconres.2018.02.006.
[41] Skarżyński Ł, Nitka M, Tejchman J. Modelling of concrete fracture at aggregate level using FEM and DEM based on X-ray μCT images of internal structure. Engng. Fract. Mech. 2015;147:13–35. https://doi.org/10.1016/j.engfracmech.2015.08.010.
[42] Nitka M, Tejchman J. Meso-mechanical modelling of damage in concrete using discrete element method with porous ITZs of defined width around aggregates. Engng. Fract. Mech. 2020;231:107029. https://doi.org/10.1016/j.engfracmech.2020.107029.
[43] Xiao J, Li W, Sun Z, Lange DA, Shah SP. Properties of interfacial transition zones in recycled aggregate concrete tested by nanoindentation. Cem. Concr. Compos. 2013;37:276–92. https://doi.org/10.1016/j.cemconcomp.2013.01.006.
[44] Xie Y, Corr DJ, Jin F, Zhou H, Shah SP. Experimental study of the interfacial transition zone (ITZ) of model rock-filled concrete (RFC). Cem. Concr. Compos. 2015;55:223–31. https://doi.org/10.1016/j.cemconcomp.2014.09.002.
[45] Combe G, Roux J-N. Discrete numerical simulation, quasistatic deformation and the origins of strain in granular materials, in. Third Int Symp Deform Charact Geomaterials, Lyon Fr 2003. https://doi.org/10.1201/noe9058096043.ch136.